

Elastoresistance as probe of strain-controlled entropy from Kondo scattering

Soumendra Nath Panja,* Jacques G Pontanel, Julian Kaiser, Anton Jesche, and Philipp Gegenwart[†]
*Experimental Physics VI, Center for Electronic Correlations and Magnetism,
 University of Augsburg, 86159 Augsburg, Germany*

(Dated: February 13, 2026)

Heavy-fermion metals are prototype correlated electron systems for the study of Kondo entanglement and quantum criticality. We use the symmetry decomposed elastoresistance to uncover the fingerprints of strain-dependent Kondo scattering as function of temperature and magnetic field in the prototypical tetragonal Kondo lattice YbRh_2Si_2 . By combining longitudinal and transverse resistance measurements under uniaxial strain applied along the tetragonal [100] and [110] directions, we obtain the elastoresistive responses in the A_{1g} , B_{1g} , and B_{2g} symmetry channels. While the responses in the symmetry-breaking channels are negligible, the isotropic A_{1g} elastoresistance displays characteristic sign changes and approaches huge values at low temperatures. Scaling analysis and comparison with linear thermal expansion measurements reveals that the elastoresistance probes the contribution of Kondo scattering to the strain dependence of magnetic entropy and signals strain-controlled quantum criticality upon cooling to 2 K.

Introduction—Uniaxial lattice strain has emerged as a uniquely powerful, symmetry-selective tuning parameter for correlated electron systems, providing direct control over electronic energy scales without introducing chemical disorder, as long as the response remains in the elastic limit of the studied material [1–4]. The elastoresistance quantifies the change of resistance with strain. When analyzed in the irreducible representations of the lattice point group, it offers a microscopic probe of how distinct symmetry components of the lattice couple to electronic degrees of freedom. Understanding how lattice symmetry governs the interplay between electronic/magnetic energy scales is a central theme in correlated electron physics. This approach uncovered divergent nematic susceptibilities in iron-based superconductors [5–11] and revealed symmetry-selective couplings in a range of correlated electron materials [12–15].

Below, we report the first study of the symmetry-resolved elastoresistance in a heavy-fermion metal. This material class is prototypical for studying correlated electron behavior, emergent orders, quantum criticality and unconventional superconductivity [16]. Heavy-fermion metals [17] are traditionally discussed within the Do-niach phase diagram [18], where the ground state is determined by the competition between Kondo screening of localized $4f$ moments and the RKKY interaction that promotes magnetic order. The antiferromagnetic (AFM) exchange between local moments and conduction electrons controlling both interactions leads to exceptionally large Grüneisen parameters [19], highlighting the strong sensitivity of these materials to pressure.

Fig. S1 sketches the generic temperature and field dependence of the electrical resistance of Kondo lattices by the black lines in the two panels. As shown in (a) the electrical resistance increases upon cooling due to the Kondo effect, passes a maximum, followed by a decrease to low temperatures, due to the formation of the correlated quasiparticle bands. This generic temperature depen-

dence scales with the Kondo temperature T_K [20–22]. In the case of crystal electric field (CEF) splitting this refers to the Kondo interaction energy with the full multiplett, which exceeds that for the lowest lying CEF level [22]. Due to the polarization of Kondo singlets in field, which leads to a reduction of the resistance, Kondo lattices often show a negative magnetoresistance below T_K , which scales like $H/(T+T_K)$ and has a form as indicated by the black line in panel (b) [23, 24]. Assuming that compressive and tensile strain ε reduces and enhances the Kondo temperature (as may be expected for the Yb case), this results in the green and blue curves, respectively. This allows to sketch the possible elastoresistance $(d\rho/d\varepsilon)/\rho$ behavior, see the red lines. Upon cooling, the elastoresistance might change its sign near T_{\max} of the ambient $\rho(T)$ curve and upon further cooling decreases to enhanced negative values (panel a), while the application of magnetic fields at low temperatures may leads to a pronounced positive elastoresistance (panel b). To explore experimentally the elastoresistance fingerprints of Kondo lattices, we focus on YbRh_2Si_2 (YRS).

YRS crystallizes in the well-known tetragonal ThCr_2Si_2 structure. It is a prototypical heavy fermion system proximate to an AFM quantum critical point (QCP), related to very weak AFM order at $T_N \approx 70$ mK [25]. Hydrostatic pressure enhances T_N and its critical magnetic field [26]. A zero-field QCP cannot be further approached, since this would require a volume expansion beyond what is possible by partial isoelectronic substitution of Si by the larger Ge in $\text{YbRh}_2(\text{Si}_{1-x}\text{Ge}_x)_2$ [27]. So far approaching the QCP requires the application of magnetic field, which however polarizes the ferromagnetic component of critical fluctuations [28]. Previously, we reported the impact of a -axis tensile and compressive strain between $-1.7 \cdot 10^{-3}$ and $+1.3 \cdot 10^{-3}$ on the resistivity maximum of YRS by electrical resistance measurements in a piezoelectric force cell (type FC100 from Razorbill) between 100 and 160 K,

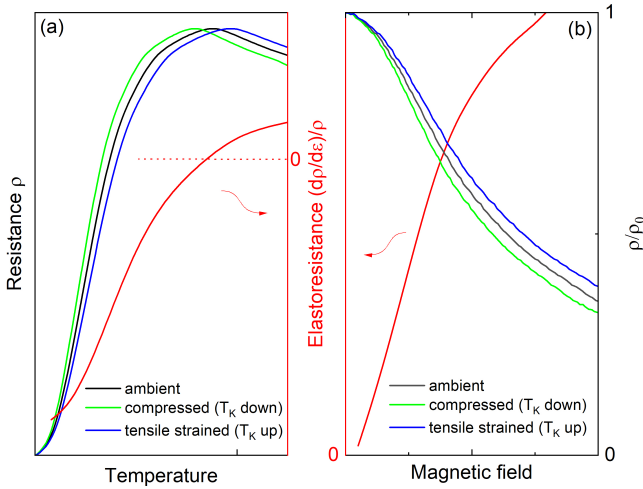


Figure 1. Schematic temperature (a) and field dependence (b) of the electrical resistance ρ of the Kondo lattice [22–24], indicated by black lines. The blue and green lines indicate the effect of an increase and decrease of T_K , respectively. The elastoresistance $(d\rho/d\epsilon)/\rho$ (in red, with right y-axis in (a) and left y-axis in (b)) is estimated under the assumption of a decrease/increase of T_K under compression/tensile strain ϵ . Note the sign change in (a) and positive elastoresistance under field in (b).

which revealed an increase of T_{\max} with tensile strain [29]. However, that study did neither investigate the temperature dependence of the elastoresistance down to low temperatures nor its anisotropy and decomposition in the contributions arising from symmetry conserving and breaking strain channels which are essential for characterizing the impact of strain on Kondo lattices.

In this Letter, we address this question through comprehensive symmetry-resolved elastoresistance measurements on tetragonal YRS. By combining longitudinal and transverse measurements under uniaxial strain applied along the in-plane [100] and [110] directions, we extract the complete elastoresistive response in the A_{1g} , B_{1g} , and B_{2g} symmetry channels for the first time in a Kondo lattice metal. We find that the response is entirely dominated by the isotropic A_{1g} channel, demonstrating that in-plane strain tunes the Kondo hybridization, with no detectable contribution from either symmetry-breaking channels, indicating the absence of nematic fluctuations. The observed temperature and field dependences are in accordance with the sketches of Fig. S1 discussed above and highlight the enormous strain dependence of the electrical resistance of Kondo lattices. Comparative measurements of the linear thermal expansion coefficient indicate that the elastoresistive scattering response tracks the strain dependence of the magnetic entropy and as such is a novel sensitive probe to characterize heavy-fermion behavior.

Methods— YRS single crystals were prepared and treated as described in [29]. Elastoresistance measure-

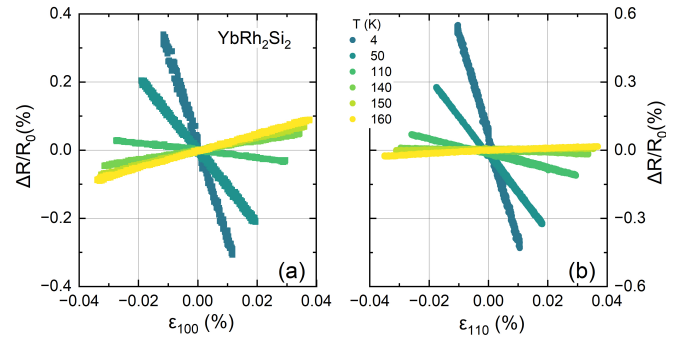


Figure 2. Longitudinal strain-induced change in electrical resistance $\Delta R/R_0$ for YRS at various temperatures for strain and current parallel to the [100] (a) and [110] (b) directions. R_0 denotes the resistance without applied strain.

ments were performed using a commercial strain cell (Razorbill Instruments CS-100) [30]. In this setup, the sample is mounted and suspended between two movable plates, with their separation precisely controlled by the applied voltage on piezoelectric stacks. Plate-like single crystals were oriented and cut with their edges in the tetragonal in-plane either along [100] or [110], with typical dimensions of approximately 2.0×0.2 to 0.6×0.05 mm³ where the shortest direction is along [001]. The samples were bonded to the strain cell using Stycast 2850FT, resulting in an effective strained length of approximately 0.8 to 1 mm. The applied strain was monitored using a built-in capacitive displacement sensor. Four-probe electrical resistance measurements as function of temperature and strain were carried out in a PPMS (Quantum Design), with the strain cell mounted on a modified P450 probe (Quantum Design). Thermal anchoring of the cell was achieved using silver foil and wires. Eight-contact configurations (as shown in Fig. S1 [31]) were employed for current flow either longitudinal or transverse to the direction of applied strain. This allows to measure simultaneously the longitudinal and transverse electrical resistance on each crystal at low temperature in magnetic fields applied parallel to strain direction. To determine the elastoresistance, isothermal sweeps of the piezo-voltage were utilized, recording the strain sensor and the electrical resistance, simultaneously.

Results and discussion— Fig. 2 shows the normalized longitudinal resistance as function of strain as $\Delta R/R_0$ with $\Delta R = R - R_0$ where R_0 denotes the resistance without applied strain for small uniaxial strain ϵ applied along the in-plane crystalline directions [100] and [110] in panels (a) and (b) respectively. Importantly all curves are linear in ϵ without noticeable hysteresis, indicating fully elastic behavior.

The strain response can be expressed through the strain derivative of the relative resistance change, $d(\Delta R/R_0)/d\epsilon$, which has been calculated fitting the linear strain response of the curves plotted in Fig. 2 for all

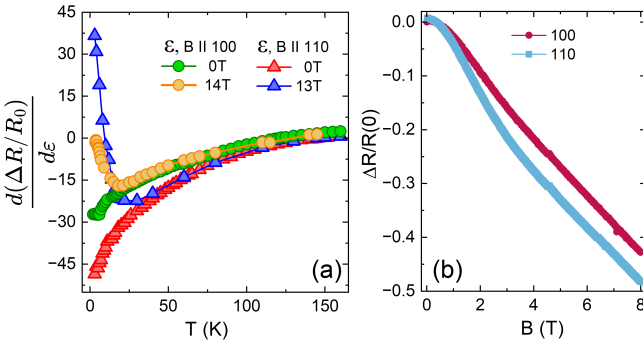


Figure 3. a): Temperature dependence of the relative resistance change under strain $d(\Delta R/R_0)/d\varepsilon$ along the [100] and [110] directions, at zero field and under applied magnetic fields. (b): Magnetoresistance $\Delta R(B)/R(0)$ for current along the [100] and [110] directions at 2 K.

measured temperatures. Generically, this property is the sum of a geometric and the intrinsic resistivity (ρ) contributions. Using $R = \rho L/A$, the geometric part reduces to $1 + 2\nu$ (cf. eq. S1 in [31]) with Poisson's ratio ν typically lying in the range $\nu \approx 0.25\text{--}0.35$ (an upper theoretical limit for any stable isotropic solid is $\nu = 0.5$). This yields a geometric contribution of approximately 1.5–1.8 [32, 33] (with a maximum possible value of 2). Any measured strain derivative that substantially differs from this baseline therefore reflects the intrinsic strain dependence of the resistivity.

Figure 3 summarizes the slope of resistance changes for uniaxial strain applied along the [100] and [110] directions. At high temperatures around 150 K, the values $\Delta R/R_0$ are almost isotropic and field independent, suggesting a dominating geometrical contribution due to the Poisson effect. The sign change for the data along the [100] direction near 120 K to negative values is consistent with our previous data plotted in Fig. 4(b) of [29] and in qualitative agreement with the expectation for Yb-based Kondo lattices, sketched in Fig. S1. The same holds for the increasingly larger negative values upon further cooling. This negative contribution is larger along [110] but our symmetry-resolved analysis presented below indicates an isotropic symmetric strain coupling. Interestingly, when a magnetic field is applied, $d(\Delta R/R_0)/d\varepsilon$ deviates from its zero-field trend below ≈ 50 K, and the effect becomes striking below ≈ 25 K. Rather than continuing its monotonic decrease, it turns upward at low temperature, rising rapidly in both orientations and even becoming positive for strain along [110], where the enhancement is strongest. Given the negative magnetoresistance at low temperatures (cf. Fig. 3(b)), the positive elastoresistance contribution in field would also be compatible with the strain dependence of T_K , sketched in Fig. S1. Overall the data demonstrate the power of elastoresistance to probe the strain dependence of Kondo-lattice interactions.

Symmetry-resolved strain measurement were performed to further characterize the elastoresistive responses. In a tetragonal crystal such as YRS, the in-plane elastic strain can be decomposed into distinct symmetry channels of the D_{4h} point group as schematically depicted in Fig. 4(f). An *isotropic* (A_{1g}) strain changes the in-plane area without breaking the fourfold (C_4) rotational symmetry; it corresponds to a uniform expansion or compression of the lattice. By contrast, B_{1g} and B_{2g} strains both break the C_4 symmetry and are therefore sensitive to nematicity. The B_{1g} channel corresponds to an *orthorhombic distortion*, characterized by stretching one axis while compressing the perpendicular one, $\varepsilon_{B1g} \sim (\varepsilon_{xx} - \varepsilon_{yy})$, whereas the B_{2g} channel represents a *shear distortion*, $\varepsilon_{B2g} \sim \varepsilon_{xy}$, which skews the lattice along the [110] and [110] diagonals. When uniaxial strain is applied along the [100] (or [110]) direction, the sample experiences $\varepsilon_{A1g+B1g}$ (or $\varepsilon_{A1g+B2g}$) strain. For strain applied along the [100] direction, the longitudinal deformation ε is accompanied by a transverse contraction $-\nu\varepsilon$, where ν is the Poisson ratio. This produces symmetry strains $\varepsilon_{A1g} = \frac{1}{2}(1 - \nu)\varepsilon$ and $\varepsilon_{B1g} = \frac{1}{2}(1 + \nu)\varepsilon$, with no shear component in the B_{2g} channel. Conversely, for strain applied along the [110] direction, the transverse response $-\nu\varepsilon$ generates $\varepsilon_{A1g} = \frac{1}{2}(1 - \nu)\varepsilon$ and a finite shear strain $\varepsilon_{B2g} = \frac{1}{2}(1 + \nu)\varepsilon$, while the B_{1g} component vanishes. The intrinsic elastoresistivity response is defined as $m_\Gamma(T, B) = \frac{1}{\rho} \frac{\partial \rho}{\partial \varepsilon_\Gamma}$, where $\Gamma = A_{1g}, B_{1g}, B_{2g}$. The sum of the longitudinal and transverse resistance changes isolates the A_{1g} channel, while their difference isolates the symmetry-breaking B_{1g} (for applied strain along [100]) or B_{2g} (for applied strain along [110]) channel. The in-plane anisotropic Poisson's ratios $\nu_{[100]} = -\varepsilon_{[010]}/\varepsilon_{[100]}$ and $\nu_{[110]} = -\varepsilon_{[\bar{1}10]}/\varepsilon_{[110]}$ relate longitudinal and transverse strain components. The explicit relations used to extract the symmetry-resolved elastoresistivity coefficients are given in Eqs. (S2)–(S5) [31]. Poisson's ratios were determined from elastic constants computed via density-functional theory (GGA); the resulting temperature-independent values are $\nu_{[100]} \approx 0.36$ and $\nu_{[110]} \approx 0.07$ [31].

To resolve the strain response into its symmetry channels, we measured the longitudinal and transverse elastoresistance using an eight-contact configuration, with four contacts allocated to each direction. Measurements were performed separately for the [100] and [110] orientations. Fig. 4 (a) and (b) show the resulting slopes of relative change in resistance $d(\Delta R/R_0)/d\varepsilon$ for current aligned parallel and perpendicular to the applied uniaxial strain along [100] and [110]. For both strain directions, the longitudinal and transverse responses follow one another closely over the entire temperature range, indicating only weak anisotropic response. Fig. 4(c) and (d) display the corresponding symmetry combinations, i.e. the sums and differences for the [100] and [110] orientations, respectively. These combinations of measurements

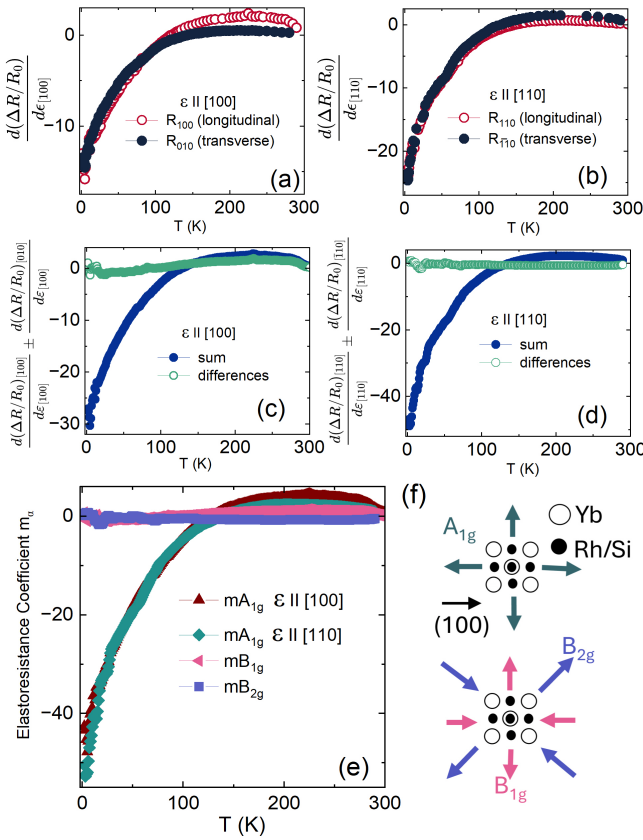


Figure 4. Symmetry decomposition of elastoresistance. (a) and (b) depict the strain derivatives of the longitudinal and transverse resistance for uniaxial strain applied along the [100] and [110] directions, respectively. (c) and (d) depict the sum and difference of longitudinal and transverse strain derivatives along [100] and [110], respectively. (e) Temperature dependence of the elastoresistance coefficients m_{A1g} , m_{B1g} , and m_{B2g} , calculated from the data in (c) and (d) using eqs. (S2)-(S5) [31]. (f) Schematic illustration of A_{1g} , B_{1g} , and B_{2g} strain symmetry channels in YRS.

isolate the couplings of the electronic system to strain in the three irreducible representations of the tetragonal point group from the geometric contribution. The extracted symmetry-resolved coefficients m_{A1g} , m_{B1g} , and m_{B2g} are shown in Fig. 4(e). Importantly, both m_{B1g} and m_{B2g} remain negligible within experimental resolution upon cooling to low temperatures, demonstrating the absence of strain induced symmetry breaking and nematic fluctuations.

On the other hand, a large negative contribution is observed in the A_{1g} channel with growing magnitude upon decreasing temperature. Remarkably the m_{A1g} data are similar when the coefficient is extracted from the [100] or [110] elastoresistance, indicating that the results are robust against systematic errors. At 2 K an enhanced value near -50 is found, whose absolute magnitude is similar to that found in hole-doped iron arsenides, which

are close to the orbital-selective Mott insulator transition [10]. However, there are striking differences in YRS: first, the sign of m_{A1g} is negative, which is related to the pressure dependence of T_K for Yb-based heavy-fermion metals as discussed above. Second, the strong temperature dependence of m_{A1g} down to the 4 K range suggests that the symmetric elastoresistance may capture the onset of quantum criticality in YRS.

Since the low- T elastoresistance of YRS is governed by the strain dependence of magnetic scattering we may apply the Fisher-Langer scaling relation $d\rho/dT \sim C$ between the magnetic specific heat and the temperature derivative of the resistance [34] and take the strain derivative on both sides. As detailed [31], this provides a relation between elastoresistance and the linear thermal expansion $\alpha_i = 1/L_i(d\Delta L_i/dT)$ (where $L_i(T)$ is the sample length along the measured direction), which probes the ϵ_i strain derivative of entropy [19]. More precisely, the scaling relation

$$\frac{\alpha_i}{T} \propto -\frac{1}{T} \int \left[\frac{1}{T} \frac{\partial}{\partial T} \left(\frac{\partial \rho}{\partial p_i} \right) \right] dT, \quad (1)$$

can be derived [10]. For the case of symmetric in-plane stress we use $(\partial \rho / \partial p_{A1g}) = -c_{A1g}^{-1} (\partial \rho / \partial \epsilon_{A1g}) = -m_{A1g} R(T) / R(300K) \cdot \rho(300K)$, with the elastic constant for symmetric in-plane stress c_{A1g} . The negative sign follows from the convention that pressure is positive under compression, whereas strain is positive under tension. Inserting to Eq. (1) yields

$$\frac{\alpha_i}{T} \propto \frac{1}{T} \int \frac{1}{T} \frac{\partial}{\partial T} \left(\frac{m_{A1g} R(T)}{R(300K)} \right) dT, \quad (2)$$

which relates the symmetric-strain elastoresistance m_{A1g} to the magnetic contribution of the expansion coefficient [10] and thus allows to check, how the elastoresistance reflects the strain dependence of magnetic entropy. For this purpose, we utilized a high-resolution capacitive dilatometer with a modified sample stage for small and very thin single crystals [35] to measure the linear thermal expansion of YRS along both the [100] and [110] direction at temperatures between 2 and 200 K.

Earlier in-plane thermal expansion measurements between 50 mK and 6 K showed a negative linear in-plane thermal expansion coefficient above T_N [36]. The negative sign of the (divergent) Grüneisen parameter indicates the decrease of T_K under pressure [37]. In the overlap regime from 2 to 6 K, our data agree well with the previous low- T experiment.

Fig. 5 shows the temperature dependence of linear thermal expansion α measured along the [100] and [110] directions. The in-plane anisotropy of α is negligible. Upon warming from 2 K it passes a minimum between 5 and 6 K and changes sign at 56 K, possibly due to the phonon contribution which is positive. For comparison,

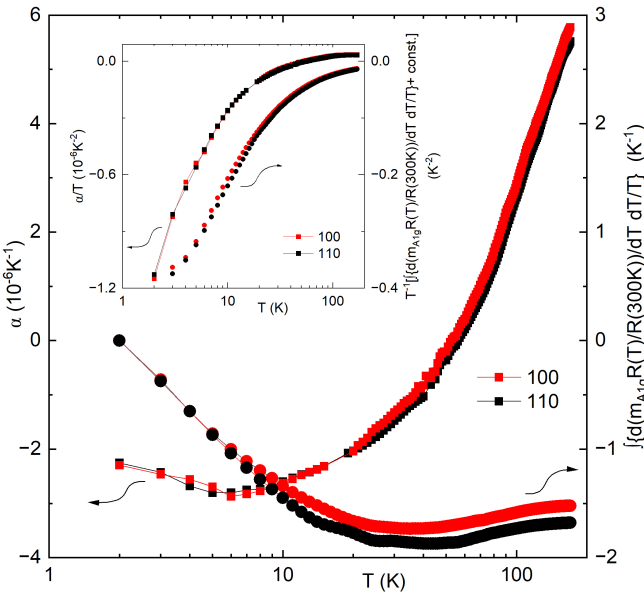


Figure 5. In-plane thermal expansion coefficient $\alpha(T)$ vs T (on log scale) for YRS measured along the [100] and [110] directions, indicated by red and black squares, respectively (left y-axis). The red and black circles display the function $\int[(dT/T)(d(m_{A1g}R/R_{300K})/dT)]$ vs T (right y-axis) with strain along the [100] (red) and [110] (black) direction. The inset displays the same thermal expansion data as α/T vs T (left y-axis) together with $T^{-1} \int[(dT/T)(d(m_{A1g}R/R_{300K})/dT)] + \text{const.}$ vs T with the integration constant as determined in [31].

we plot the corresponding ‘‘Fisher-Langer thermal expansion coefficients’’ calculated from integrating the temperature derivative of the resistance change with symmetry conserving in-plane strain. Its negative sign is indeed in accordance with that of α , indicating that the (strain dependent) electrical resistance probes the strain dependence of magnetic entropy. The inset compares α/T with the right side of Eq. (2), where an integration constant was added with the assumption that ‘‘Fisher’s thermal expansion’’ linearly approaches zero at $T = 0$ [31]. Interestingly, both properties display a negatively divergent behavior below about 50 K. This strongly motivates subsequent milli-Kelvin experiments to probe quantum criticality with the elastoresistance.

More generally, the correspondence between the two curves demonstrates that the prototypical Kondo lattice YRS displays a hugely enhanced symmetric elastoresistance, whose sign and temperature dependence reflects the strain dependence of the magnetic entropy. In contrast to iron-pnictides, nematic fluctuations do not play a role in YRS and the sign of the elastoresistance is negative, reflecting the fact that in Yb-based heavy-fermion metals the Kondo temperature is reduced by strain. Furthermore, in contrast to the case of the most correlated iron pnictide CsFe_2As_2 which shows huge positive elastoresistance and a Fermi liquid behavior below 10 K in

$\alpha(T)$ [10], the data on YRS indicate non-Fermi liquid behavior in these properties with a divergent A_{1g} strain sensitivity upon cooling.

Conclusions— We have performed symmetry-resolved elastoresistance measurements on the archetypal heavy-fermion metal YbRh_2Si_2 to determine how in-plane strain couples to its low-energy electronic and magnetic properties. A huge negative elastoresistance with a positive field-induced contribution is found at low temperatures. This behavior, illustrated in Fig. S1, shall be generic for Yb-based Kondo lattices. Longitudinal and transverse electrical resistance measurements under uniaxial strain along [100] and [110] confirmed the above qualitative expectation and revealed the quantitative elastoresistive response which is overwhelmingly dominated by the isotropic A_{1g} channel, which upon cooling to 2 K reaches huge values of order -50 . The absence of detectable B_{1g} and B_{2g} responses shows that in-plane strain exclusively tunes the overall Kondo hybridization without inducing symmetry-breaking electronic and structural distortions. The close correspondence between the A_{1g} elastoresistance and the in-plane thermal expansion establishes a direct link to the strain dependence of the magnetic entropy, highlighting elastoresistance as a novel tool to probe the coupling of conduction electrons to the strain dependent magnetic correlations in heavy-fermion metals. Previously, we demonstrated that tensile strain can tune T_K of YRS to the value required for approaching the extrapolated zero-field quantum critical point. Symmetry-resolved elastoresistance measurements at large tensile strain and down to the milli-Kelvin range are thus of huge interest to uncover the nature of its quantum critical state, avoiding additional complexity associated with magnetic field polarization of ferromagnetic fluctuations near the critical field or disorder in chemically substituted YRS [28, 38].

Acknowledgments—We acknowledge fruitful discussions with A. E. Böhmer and G. Zwicknagl. S.N.P. was supported by the Alexander von Humboldt Foundation.

* soumendra.panja@uni-a.de

† philipp.gegenwart@uni-a.de

- [1] C. W. Hicks, F. Jerzembeck, H. M. Noad, M. E. Barber, and A. P. Mackenzie, Probing quantum materials with uniaxial stress, *Annu. Rev. Condens. Matter Phys.* **16**, 417 (2025).
- [2] N. Hyun Jo, E. Gati, and H. Pfau, Uniaxial stress effect on the electronic structure of quantum materials, *Front. Electron. Mater.* **4**, 1392760 (2024).
- [3] J. Wang, M. Spitaler, Y.-S. Su, K. Zoch, C. Krellner, P. Puphal, S. Brown, and A. Pustogow, Controlled Frustration Release on the Kagome Lattice by Uniaxial-Strain Tuning, *Phys. Rev. Lett.* **131**, 256501 (2023).
- [4] F. Lieberich, Y. Saito, Y. Agarmani, T. Sasaki, N. Yoneyama, S. M. Winter, M. Lang, and E. Gati, Prob-

ing and tuning geometric frustration in an organic quantum magnet via elastocaloric measurements under strain, *Sci. Adv.* **11**, eadz0699 (2025).

[5] J.-H. Chu, H.-H. Kuo, J. G. Analytis, and I. R. Fisher, Divergent Nematic Susceptibility in an Iron Arsenide Superconductor, *Science* **337**, 710 (2012).

[6] H.-H. Kuo, J.-H. Chu, J. C. Palmstrom, S. A. Kivelson, and I. R. Fisher, Ubiquitous signatures of nematic quantum criticality in optimally doped Fe-based superconductors, *Science* **352**, 958 (2016).

[7] S. Hosoi, K. Matsuura, K. Ishida, H. Wang, Y. Mizukami, T. Watashige, S. Kasahara, Y. Matsuda, and T. Shibauchi, Nematic quantum critical point without magnetism in $\text{FeSe}_{1-x}\text{S}_x$ superconductors, *PNAS* **113**, 81390 (2016).

[8] K. Ishida, M. Tsujii, S. Hosoi, Y. Mizukami, S. Ishida, A. Iyo, H. Eisaki, T. Wolf, K. Grube, H. v. Löhneysen, R. M. Fernandes, and T. Shibauchi, Novel electronic nematicity in heavily hole-doped iron pnictide superconductors, *PNAS* **117**, 6424 (2020).

[9] P. Wiecki, A.-A. Haghaghirad, F. Weber, M. Merz, R. Heid, and A. E. Böhmer, Dominant In-Plane Symmetric Elastoresistance in CsFe_2As_2 , *Phys. Rev. Lett.* **125**, 187001 (2020).

[10] P. Wiecki, M. Frachet, A.-A. Haghaghirad, T. Wolf, C. Meingast, R. Heid, and A. E. Böhmer, Emerging symmetric strain response and weakening nematic fluctuations in strongly hole-doped iron-based superconductors, *Nat. Commun.* **12**, 4824 (2021).

[11] T. Worasaran, M. S. Ikeda, J. C. Palmstrom, J. A. W. Straquadine, S. A. Kivelson, and I. R. Fisher, Nematic quantum criticality in an Fe-based superconductor revealed by strain-tuning, *Science* **372**, 973 (2021).

[12] E. W. Rosenberg, J.-H. Chu, J. P. C. Ruff, and I. R. Fisher, Divergence of the quadrupole-strain susceptibility of the electronic nematic system YbRu_2Ge_2 , *PNAS* **116**, 7232 (2019).

[13] L. Ye, Y. Sun, V. Sunko, and I. R. Fisher, Elastocaloric signatures of symmetric and antisymmetric strain-tuning of quadrupolar and magnetic phases in DyB_2C_2 , *PNAS* **120**, e2302800120 (2023).

[14] L. Ye, M. E. Sorensen, M. D. Bachmann, and I. R. Fisher, Measurement of the magnetic octupole susceptibility of $\text{PrV}_2\text{Al}_{20}$, *Nat. Commun.* **15**, 7005 (2024).

[15] E. W. Rosenberg, M. Ikeda, and I. R. Fisher, The nematic susceptibility of the ferroquadrupolar metal TmAg_2 measured via the elastocaloric effect, *npj Quantum Mater.* **9**, 46 (2024).

[16] P. Gegenwart, Q. Si, and F. Steglich, Quantum criticality in heavy-fermion metals, *Nat. Phys.* **4**, 186 (2008).

[17] G. R. Stewart, Heavy-fermion systems, *Rev. Mod. Phys.* **56**, 755 (1984).

[18] S. Doniach, The kondo lattice and weak antiferromagnetism, *Physica B+C* **91**, 231 (1977).

[19] P. Gegenwart, Grüneisen parameter studies on heavy fermion quantum criticality, *Rep. Prog. Phys.* **79**, 114502 (2016).

[20] M. Lavagna, C. Lacroix, and M. Cyrot, Electrical resistivity of the kondo lattice, *J. Appl. Phys.* **53**, 2055 (1982).

[21] P. Coleman, Constrained quasiparticles and conduction in heavy-fermion systems, *Phys. Rev. Lett.* **59**, 10265 (1987).

[22] D. L. Cox and N. Grewe, Transport properties of the anderson lattice, *Z. Phys. B* **71**, 321 (1988).

[23] P. Schlottmann, Bethe-Ansatz Solution of the Ground-State of the $\text{SU}(2j+1)$ Kondo(Coqblin-Schrieffer) Model: Magnetization, Magnetoresistance and Universality, *Z. Phys. B* **51**, 223 (1983).

[24] B. Batlogg, D. Bishop, E. Bucher, B. Golding, A. Ramirez, Z. Fisk, J. Smith, and H. Ott, Superconductivity and Heavy Fermions, *J. Magn. Magn. Mater.* **63**, 441 (1987).

[25] P. Gegenwart, J. Custers, C. Geibel, K. Neumaier, T. Tayama, K. Tenya, O. Trovarelli, and F. Steglich, Magnetic-Field Induced Quantum Critical Point in YbRh_2Si_2 , *Phys. Rev. Lett.* **89**, 056402 (2002).

[26] Y. Tokiwa, P. Gegenwart, T. Radu, J. Ferstl, G. Sparn, C. Geibel, and F. Steglich, Field-Induced Suppression of the Heavy-Fermion State in YbRh_2Si_2 , *Phys. Rev. Lett.* **94**, 226402 (2005).

[27] J. Custers, P. Gegenwart, H. Wilhelm, K. Neumaier, Y. Tokiwa, O. Trovarelli, C. Geibel, F. Steglich, C. Pépin, and P. Coleman, The break-up of heavy electrons at a quantum critical point, *Nature* **424**, 524 (2003).

[28] P. Gegenwart, J. Custers, Y. Tokiwa, C. Geibel, and F. Steglich, Ferromagnetic Quantum Critical Fluctuations in $\text{YbRh}_2(\text{Si}_{0.95}\text{Ge}_{0.05})_2$, *Phys. Rev. Lett.* **94**, 076402 (2005).

[29] S. N. Panja, A. Jesche, N. Tang, and P. Gegenwart, Tensile and compressive strain tuning of a kondo lattice, *Phys. Rev. B* **109**, 205152 (2024).

[30] C. W. Hicks, M. E. Barber, S. D. Edkins, D. O. Brodsky, and A. P. Mackenzie, Piezoelectric-based apparatus for strain tuning, *Rev. Sci. Instrum.* **85**, 065003 (2014).

[31] See supplementary material, for additional experimental details and data analysis including Refs. [9, 30, 34, 35, 39, 40].

[32] W. D. Callister and D. G. Rethwisch, *Materials Science and Engineering: An Introduction*, 10th ed. (Wiley, Hoboken, NJ, 2018).

[33] Y. Sun, S. Thompson, and T. Nishida, *Strain Effect in Semiconductors: Theory and Device Applications* (Springer, New York, 2010).

[34] M. E. Fisher and J. S. Langer, Resistive anomalies at magnetic critical points, *Phys. Rev. Lett.* **20**, 665 (1968).

[35] R. Küchler, S. Panja, S. Wirth, and P. Gegenwart, High-resolution capacitance dilatometry of microscopically thin samples using the world's smallest dilatometer, *Rev. Sci. Instr.* **97**, 025209 (2026).

[36] R. Küchler, F. Weickert, P. Gegenwart, N. Oeschler, J. Ferstl, C. Geibel, and F. Steglich, Low-temperature thermal expansion and magnetostriction of $\text{YbRh}_2(\text{Si}_{1-x}\text{Ge}_x)_2$ ($x = 0$ and 0.05), *J. Magn. Magn. Mater.* **272-276**, 229 (2004).

[37] R. Küchler, N. Oeschler, P. Gegenwart, T. Cichorek, K. Neumaier, O. Tegus, C. Geibel, J. Mydosh, F. Steglich, L. Zhu, and Q. Si, Divergence of the Grüneisen Ratio at Quantum Critical Points in Heavy Fermion Metals, *Phys. Rev. Lett.* **91**, 066405 (2003).

[38] M.-H. Schubert, Y. Tokiwa, S.-H. Hübner, M. Mchalwat, E. Blumenröther, H. S. Jeevan, and P. Gegenwart, Tuning low-energy scales in YbRh_2Si_2 by non-isoelectronic substitution and pressure, *Phys. Rev. Res.* **1**, 032004(R) (2019).

[39] M. de Jong, W. Chen, T. Angsten, A. Jain, R. Notesline, A. Gamst, M. Sluiter, C. Krishna Ande, S. van der Zwaag, J. J. Plata, C. Toher, S. Curtarolo, G. Ceder, K. A. Persson, and M. Asta, Charting the complete elas-

tic properties of inorganic crystalline compounds, *Sci. Data* **2**, 150009 (2015).

[40] R. Küchler, T. Bauer, M. Brando, and F. Steglich, A compact and miniaturized high resolution capacitance dilatometer for measuring thermal expansion and magnetostriction, *Rev. Sci. Instrum.* **83**, 095102 (2012).

SUPPLEMENTAL MATERIAL

Eight electrical contacts were put on the bar-shaped, cut and polished crystal. Four contacts were aligned with the applied strain direction to measure the longitudinal elastoresistance, and four more contacts were oriented perpendicular to the strain direction to measure the transverse response, as shown in Fig. S1. Uniaxial strain is applied along the horizontal direction ε_{xx} ($\varepsilon \parallel 100/110$), and the resulting transverse strain ε_{yy} ($\varepsilon \parallel 010/1\bar{1}0$) follows the Poisson relation $\varepsilon_{yy} = -\nu \varepsilon_{xx}$. This eight-contact configuration allows simultaneous measurement of the longitudinal and transverse strain responses, enabling extraction of the elastoresistivity in the A_{1g} , B_{1g} , and B_{2g} symmetry channels.

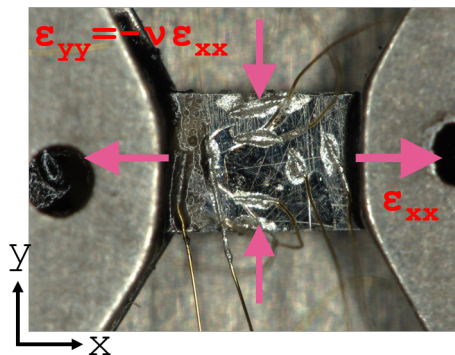


Figure S1. Photograph of a YbRh_2Si_2 crystal mounted on a CS-100 Razorbill strain device with four longitudinal and four transverse electrical contacts for elastoresistance measurements.

Below we show how the longitudinal and transverse elastoresistance measurements can be combined to extract the elastoresistance coefficients along the A_{1g} , B_{1g} , and B_{2g} symmetry channels. For uniaxial strain ε applied along a given crystallographic direction, the measured fractional change in resistance is

$$\frac{\Delta R}{R_0} = \frac{\Delta \rho}{\rho_0} + (1 + 2\nu) \varepsilon \quad (0.1)$$

The first term of Eq. S1 describes the intrinsic contribution to elastoresistance and second term is due to the contribution from geometry. For strain applied along x (e.g., $\varepsilon_{xx} = 100$), the longitudinal and transverse strain components are

$$\varepsilon_{xx} = \varepsilon \quad \varepsilon_{yy} = \varepsilon_{zz} = -\nu \varepsilon.$$

The resulting area change is

$$\frac{\Delta A}{A} \simeq \varepsilon_{yy} + \varepsilon_{zz} = -2\nu \varepsilon$$

leading to a geometric contribution

$$\left(\frac{\Delta R}{R_0} \right)_{\text{geom}} = \frac{\Delta L}{L} - \frac{\Delta A}{A} = \varepsilon + 2\nu \varepsilon = (1 + 2\nu) \varepsilon$$

In tetragonal symmetry with applied strain along 100:

$$A_{1g} \text{ strain (isotropic): } \varepsilon_{A_{1g}} = \frac{1}{2}(\varepsilon_{xx} + \varepsilon_{yy}) = \frac{1}{2}(\varepsilon - \nu\varepsilon) = \frac{1}{2}(1 - \nu)\varepsilon$$

$$B_{1g} \text{ strain (x-y): } \varepsilon_{B_{1g}} = \frac{1}{2}(\varepsilon_{xx} - \varepsilon_{yy}) = \frac{1}{2}(\varepsilon + \nu\varepsilon) = \frac{1}{2}(1 + \nu)\varepsilon$$

$$B_{2g} \text{ strain: } \varepsilon_{B_{2g}} = \varepsilon_{xy} = 0$$

Uniaxial strain applied along [100] decomposes into a mixture of A_{1g} and B_{1g} symmetry components. The corresponding elastoresistive response is

$$\frac{\Delta\rho}{\rho_0} = m_{A_{1g}}\varepsilon_{A_{1g}} + m_{B_{1g}}\varepsilon_{B_{1g}}$$

$$\frac{\Delta\rho}{\rho_0} = m_{A_{1g}}\left[\frac{1}{2}(1 - \nu)\varepsilon\right] + m_{B_{1g}}\left[\frac{1}{2}(1 + \nu)\varepsilon\right]$$

$$\frac{\Delta\rho}{\rho_0} = \varepsilon\left[m_{A_{1g}}\frac{1 - \nu}{2} + m_{B_{1g}}\frac{1 + \nu}{2}\right]$$

Including both geometry factor and intrinsic response, longitudinal change in resistance under [100] strain,

$$\frac{d}{d\varepsilon_{[100]}}\left(\frac{\Delta R}{R_0}\right)_{[100]} = (1 + 2\nu_{[100]}) + m_{A_{1g}}\left(\frac{1 - \nu_{[100]}}{2}\right) + m_{B_{1g}}\left(\frac{1 + \nu_{[100]}}{2}\right)$$

while the corresponding transverse response is

$$\frac{d}{d\varepsilon_{[100]}}\left(\frac{\Delta R}{R_0}\right)_{[010]} = (1 + 2\nu_{[100]}) + m_{A_{1g}}\left(\frac{1 - \nu_{[100]}}{2}\right) - m_{B_{1g}}\left(\frac{1 + \nu_{[100]}}{2}\right)$$

The geometric factor $(1 + 2\nu_{[100]})$ is therefore identical in both channels and cancels in the subtraction of the symmetry combinations as given by Eq. S3. For the A_{1g} (sum) combination, the geometric gauge factor does not cancel. Purely geometric contribution $(1 + 2\nu)$ enters the longitudinal and transverse responses with the same sign and therefore adds in the sum. Thus, to obtain the intrinsic A_{1g} elastoresistive coefficient one must either (i) explicitly subtract the geometric term using ν , or (ii) define $m_{A_{1g}}$ from the outset to denote the geometry-subtracted (intrinsic) quantity. After this subtraction, the remaining dependence on ν appears only through the prefactor $1/(1 - \nu)$ that converts the applied uniaxial strain to the symmetry-resolved A_{1g} strain component; this factor is not a geometric contribution. Combining the longitudinal and transverse responses derived above, we can extract the symmetry-resolved elastoresistivity coefficients. Hence, the elastoresistance coefficient along the symmetry channel $m_{A_{1g}}$ and $m_{B_{1g}}$ are:

$$m_{A_{1g}} = \frac{1}{1 - \nu_{[100]}} \left[\frac{d(\Delta R/R_0)_{[100]}}{d\varepsilon_{[100]}} + \frac{d(\Delta R/R_0)_{[010]}}{d\varepsilon_{[100]}} \right] \quad (0.2)$$

$$m_{B_{1g}} = \frac{1}{1 + \nu_{[100]}} \left[\frac{d(\Delta R/R_0)_{[100]}}{d\varepsilon_{[100]}} - \frac{d(\Delta R/R_0)_{[010]}}{d\varepsilon_{[100]}} \right] \quad (0.3)$$

An entirely analogous procedure applies for uniaxial strain along [110], where the response mixes A_{1g} and B_{2g}

symmetries. The longitudinal and transverse change in resistance for uniaxial strain along [110] are:

$$\begin{aligned}\frac{d}{d\varepsilon_{[110]}}\left(\frac{\Delta R}{R_0}\right)_{[110]} &= (1 + 2\nu_{[110]}) + m_{A_{1g}}\left(\frac{1 - \nu_{[110]}}{2}\right) + m_{B_{2g}}\left(\frac{1 + \nu_{[110]}}{2}\right) \\ \frac{d}{d\varepsilon_{[110]}}\left(\frac{\Delta R}{R_0}\right)_{[\bar{1}10]} &= (1 + 2\nu_{[110]}) + m_{A_{1g}}\left(\frac{1 - \nu_{[110]}}{2}\right) - m_{B_{2g}}\left(\frac{1 + \nu_{[110]}}{2}\right)\end{aligned}$$

After subtracting the common geometric term, summing and subtracting results the elastoresistance coefficients for the symmetry channel $m_{A_{1g}}$ and $m_{B_{2g}}$ are:

$$m_{A_{1g}} = \frac{1}{1 - \nu_{[110]}} \left[\frac{d(\Delta R/R_0)_{[110]}}{d\varepsilon_{[110]}} + \frac{d(\Delta R/R_0)_{[\bar{1}10]}}{d\varepsilon_{[110]}} \right] \quad (0.4)$$

$$m_{B_{2g}} = \frac{1}{1 + \nu_{[110]}} \left[\frac{d(\Delta R/R_0)_{[110]}}{d\varepsilon_{[110]}} - \frac{d(\Delta R/R_0)_{[\bar{1}10]}}{d\varepsilon_{[110]}} \right]. \quad (0.5)$$

Equations 0.2 and 0.4 are the relations providing two independent determinations of $m_{A_{1g}}$, serving as an internal consistency check on the analysis.

IN-PLANE POISSON'S RATIO

For a tetragonal crystal of symmetry , the elastic stiffness tensor in Voigt notation is

$$C = \begin{pmatrix} C_{11} & C_{12} & C_{13} & 0 & 0 & 0 \\ C_{12} & C_{11} & C_{13} & 0 & 0 & 0 \\ C_{13} & C_{13} & C_{33} & 0 & 0 & 0 \\ 0 & 0 & 0 & C_{44} & 0 & 0 \\ 0 & 0 & 0 & 0 & C_{44} & 0 \\ 0 & 0 & 0 & 0 & 0 & C_{66} \end{pmatrix}$$

For a tetragonal system with independent stiffness coefficients Poisson's ratios along 100 and 110 are:

$$\nu_{[100]} = \frac{C_{13}^2 - C_{12}C_{33}}{C_{13}^2 - C_{11}C_{33}}$$

$$\nu_{[110]} = \frac{C_{33}(C_{11} + C_{12} - 2C_{66}) - 2C_{13}^2}{C_{33}(C_{11} + C_{12} + 2C_{66}) - 2C_{13}^2}$$

The elastic tensor for YbRh_2Si_2 has been obtained from density-functional theory (DFT) within the generalized-gradient approximation [39]. The obtained values (in GPa) form the following Voigt stiffness matrix:

$$C_{ij} = \begin{pmatrix} 229 & 104 & 83 & 0 & 0 & 0 \\ 104 & 229 & 83 & 0 & 0 & 0 \\ 83 & 83 & 212 & 0 & 0 & 0 \\ 0 & 0 & 0 & 69 & 0 & 0 \\ 0 & 0 & 0 & 0 & 69 & 0 \\ 0 & 0 & 0 & 0 & 0 & 116 \end{pmatrix}$$

The elastic tensor yields a Poisson's ratio of approximately $\nu_{[100]} \approx 0.36$ [100], and $\nu_{[110]} \approx 0.07$.

EFFECT OF OUT-OF-PLANE (*c*-AXIS) COMPRESSION

The expressions in Eqs. (S2-S5) were obtained under the assumption that only in-plane strain components contribute to the elastoresistance. This approximation is natural for an in-plane transport geometry and is sufficient to establish the symmetry decomposition and the extraction procedure for the A_{1g} , B_{1g} , and B_{2g} channels. However, a uniaxial in-plane strain ($\varepsilon_{\parallel} = \varepsilon_{[100]}$ or $\varepsilon_{[110]}$) in a tetragonal crystal inevitably generates an accompanying out-of-plane strain ε_{zz} through the directional Poisson ratio ν' , defined as $\nu' = -\varepsilon_{zz}/\varepsilon_{\parallel}$. This out-of-plane deformation is fully symmetric and therefore transforms as A_{1g} , contributing an additional isotropic strain component that must be included in the complete elastoresistance response.

For a uniaxial in-plane strain ε_{\parallel} , the symmetric in-plane A_{1g} strain appearing in Eqs. (S2) and (S4), given by $(1 - \nu)\varepsilon_{\parallel}/2$, must be combined with the out-of-plane symmetric contribution $-\nu'\varepsilon_{\parallel}$. The total A_{1g} strain entering the elastoresistance is thus the sum of these two contributions.

$$\varepsilon_{A_{1g}}^{(\text{total})} = \left(\frac{1 - \nu}{2} - \nu' \right) \varepsilon_{\parallel}$$

For uniaxial strain along [100] the longitudinal and transverse change in resistance including *c* axis compression are now expressed as

$$\begin{aligned} \frac{d}{d\varepsilon_{[100]}} \left(\frac{\Delta R}{R_0} \right)_{[100]} &= (1 + 2\nu_{[100]}) + m_{A_{1g}} \left(\frac{1 - \nu_{[100]}}{2} - \nu'_{[100]} \right) + m_{B_{1g}} \left(\frac{1 + \nu_{[100]}}{2} \right), \\ \frac{d}{d\varepsilon_{[100]}} \left(\frac{\Delta R}{R_0} \right)_{[010]} &= (1 + 2\nu_{[100]}) + m_{A_{1g}} \left(\frac{1 - \nu_{[100]}}{2} - \nu'_{[100]} \right) - m_{B_{1g}} \left(\frac{1 + \nu_{[100]}}{2} \right) \end{aligned}$$

Summing and subtracting these expressions now yields

$$\begin{aligned} \frac{d(\Delta R/R_0)_{[100]}}{d\varepsilon_{[100]}} + \frac{d(\Delta R/R_0)_{[010]}}{d\varepsilon_{[100]}} &= 2(1 + 2\nu_{[100]}) + 2m_{A_{1g}} \left(\frac{1 - \nu_{[100]}}{2} - \nu'_{[100]} \right) \\ \frac{d(\Delta R/R_0)_{[100]}}{d\varepsilon_{[100]}} - \frac{d(\Delta R/R_0)_{[010]}}{d\varepsilon_{[100]}} &= 2m_{B_{1g}} \left(\frac{1 + \nu_{[100]}}{2} \right) \end{aligned}$$

Demonstrating explicitly that the B_{1g} and B_{2g} channel is unaffected by the out-of-plane Poisson response, while excluding the geometric contribution the elastoresistance coefficient in A_{1g} becomes

$$m_{A_{1g}} = \frac{\frac{d(\Delta R/R_0)_{[100]}}{d\varepsilon_{[100]}} + \frac{d(\Delta R/R_0)_{[010]}}{d\varepsilon_{[100]}}}{1 - \nu_{[100]} - 2\nu'_{[100]}} \quad (0.6)$$

Comparison with Eq. (S2) shows that the only change required to account for *c*-axis compression is the replacement

$$1 - \nu_{[100]} \longrightarrow 1 - \nu_{[100]} - 2\nu'_{[100]}$$

An entirely analogous modification applies for uniaxial strain along [110], where the in-plane response mixes A_{1g} and B_{2g} symmetries, leaving the B_{2g} channel unchanged but renormalizing the A_{1g} term in precisely the same manner as for applied strain along [100].

Because both the in-plane symmetric strain and the Poisson-driven out-of-plane strain transform as A_{1g} , their contributions enter with the same symmetry and cannot be disentangled experimentally. Thus our measured $m_{A_{1g}}$ response therefore contains the combined response to symmetric in-plane biaxial strain and the accompanying unavoidable *c*-axis compression.

EFFECT OF REDUCED STRAIN-TRANSFER EFFICIENCY

The elastoresistance coefficients reported here were obtained using the displacement measured by the capacitance sensor of the CS-100 strain cell. Because the strain cell has finite mechanical compliance, part of the actuator motion is accommodated by elastic deformation and a small rotation of the cell rather than by uniform deformation of the sample itself. As a result, the displacement inferred from the capacitance sensor slightly overestimates the true strain experienced by the crystal. This effect can be captured by introducing an effective strain-calibration factor $\eta < 1$, such that the actual strain in the sample is reduced relative to the nominal applied strain. Consequently, the measured elastoresistance coefficients underestimate the true values by a constant factor $1/\eta$. Since this correction arises from the static mechanical properties and geometry of the strain cell, η is independent of temperature and magnetic field, so that all elastoresistance curves are uniformly rescaled while their relative temperature and field dependences remain unchanged. The elastoresistance slopes shown in Fig. 3(a) were extracted under the assumption of 100% strain transfer between the piezoelectric actuator and the YbRh_2Si_2 crystal. If the actual strain transferred to the sample is reduced, the extracted coefficients must be renormalized. For a strain-transfer efficiency η , the strain in the crystal is $\varepsilon_{\text{sample}} = \eta \varepsilon_{\text{applied}}$, so that elastoresistance coefficient

$$m_{\text{true}}(T, B) = \frac{d(\Delta R/R_0)}{d\varepsilon_{\text{sample}}} = \frac{1}{\eta} \frac{d(\Delta R/R_0)}{d\varepsilon_{\text{applied}}} = \frac{m_{\text{meas}}(T, B)}{\eta}.$$

η is expected to be between 0.6–0.8 for the utilized strain device [30]; the exact value does not affect conclusions. For instance $\eta = 0.70$ results

$$m_{\text{true}}(T, B) \simeq 1.43 m_{\text{meas}}(T, B).$$

Thus, every curve in Fig. 3(a) would be uniformly rescaled upward by a factor $1/\eta$, while the temperature and field dependence of the data remain unchanged. Only the absolute magnitude of the elastoresistivity is modified by the reduced strain transfer. Because the rescaling is uniform, the relative enhancement of $m(T)$ is unaffected. For example, the increase from $m \sim 2$ at high temperature to $m \sim 45$ at low temperature simply becomes $m \sim 3$ to $m \sim 64$ for $\eta = 0.70$, leaving the percent change unchanged. Uncertainties in strain-transfer efficiency therefore alter only the overall scale of $m(T)$ and do not influence the qualitative or quantitative trends discussed in the text.

LINEARITY OF THE ELASTORESISTANCE AT LARGE STRAIN

As discussed in the main text, elastoresistance measurements were generally performed within a narrow strain window centered near the nominal zero-strain/strain neutral point, typically $\varepsilon_{xx} = \pm 0.04\%$ [Fig. 2 of the main text]. Within this restricted strain range, the resistance varies strictly linearly with strain, allowing the elastoresistance coefficients to be extracted reliably from the slope. Here, the strain-neutral point is defined as the reference strain corresponding to zero voltage applied to the piezostacks of the Razorbill device. Strain sweeps are performed about this point, within a regime where the resistance–strain response is locally linear and symmetric. This strain-neutral point does not necessarily coincide with the *true* zero-strain condition, as it can be shifted by differential thermal contraction during thermal cycling. To verify that the extracted elastoresistance coefficients are not sensitive to the choice of this reference point, we performed additional measurements at $T = 80$ K over a much wider strain range. Specifically, small-amplitude strain sweeps were carried out about multiple centre positions spanning a total range exceeding compressive strain $\varepsilon_{xx} = -0.1\%$, as shown in Fig. S2. At each center position, the resistance remains linear over the local sweep range, and the extracted slope is found to be independent of the absolute strain offset. This demonstrates that the elastoresistance is governed by the local linear response and does not depend on the precise value chosen as the zero-strain reference.

These measurements confirm that the elastoresistance coefficients reported in the main text reflect an intrinsic linear response of the system and are not affected by residual strain offsets or by the absolute strain level within the investigated range. The restriction to small strain amplitudes in the main text therefore ensures operation well within the linear-response regime while yielding results that are representative of the broader strain behavior.

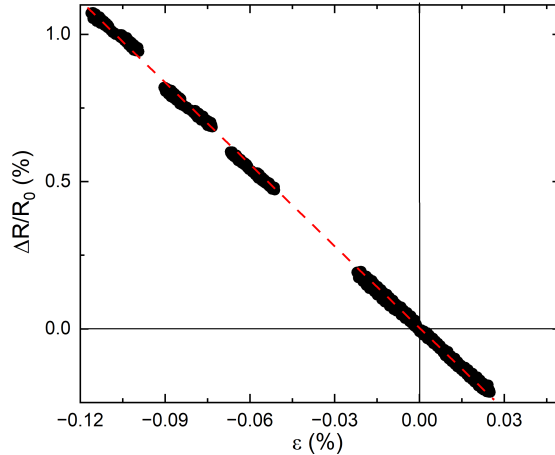


Figure S2. Percentage change in strain driven resistance $\Delta R/R_0$ as a function of uniaxial strain ε measured along the same crystallographic direction as in the main text, shown over an extended strain range. The red dashed line is a linear fit to the data, demonstrating that the elastoresistance remains linear up to the maximum applied compressive strain of $\sim 0.12\%$. This extended-range plot confirms that the elastoresistance coefficients reported in the main text are not affected by nonlinear strain response.

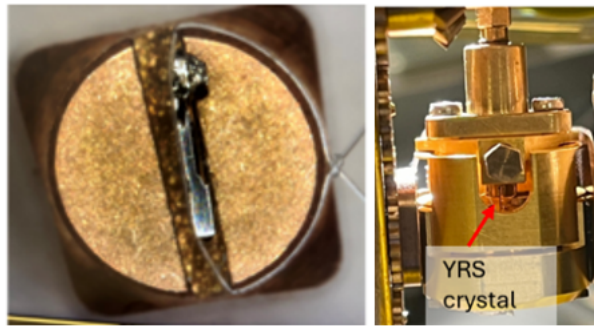


Figure S3. (a) YbRh_2Si_2 single crystal secured with a PTFE thread and mounted on a slotted sample stage for measurements using a capacitive dilatometer. Such mounting facilitates the handling and reliable positioning of thin, fragile crystals while ensuring good mechanical stability during measurement. (b) The same YbRh_2Si_2 crystal mounted inside the capacitive dilatometer prior to measurement, illustrating the final experimental configuration.

IN-PLANE THERMAL EXPANSION MEASUREMENT ON THIN YbRh_2Si_2 PLATELETS

Capacitive dilatometry provides high-resolution access to temperature induced length changes along selected crystallographic directions. In capacitive dilatometers, a specimen is positioned against the movable electrode and secured using a mechanical clamping mechanism [40]. This configuration requires samples that are sufficiently rigid and self-supporting, typically with thickness of millimeter-scale dimensions, in order to stand the crystal upright and mechanical stability during installation. As a result, extremely thin or mechanically delicate samples cannot be mounted reproducibly using standard methods with thicknesses of the order of a few hundred of micrometers. Here, we employ our recently developed novel sample-mounting strategy [35] using slotted mounting stamp (see Fig. S3) that overcomes these constraints and, for the first time, enables direct reliable measurements of the thermal expansion along the in-plane 100 and 110 crystallographic directions of a thin platelet single crystal of YbRh_2Si_2 . In a capacitive dilatometer, the measured length change contains not only the intrinsic thermal expansion of the sample but also a contribution from the dilatometer, arising from the thermal expansion of the Be-Cu cell body itself. To isolate the sample response, a background subtraction procedure is required. The cell contribution is determined by combining a direct measurement of the empty-cell response with literature thermal expansion data of copper [40].

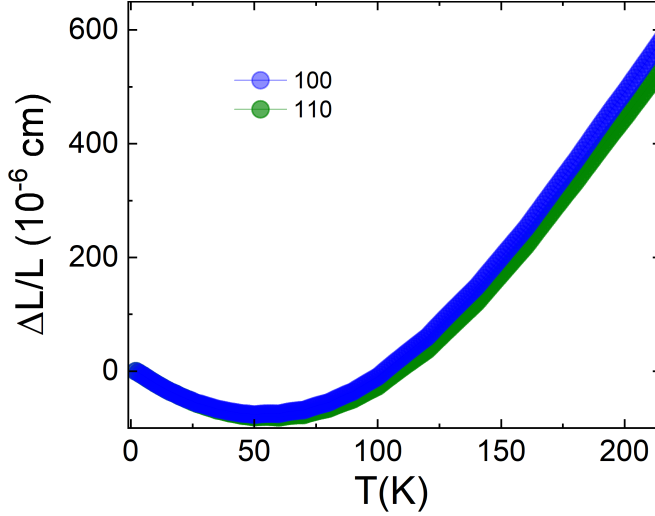


Figure S4. The relative length change $\Delta L/L_0$ of a YbRh_2Si_2 single crystal along 100 and 110 crystallographic direction.

The intrinsic relative length change of the sample is then obtained as

$$\left(\frac{\Delta L}{L_0}\right)_{\text{sample}} = \frac{\Delta L_{\text{sample}}^{\text{meas}}(T) - \Delta L_{\text{empty cell}}(T)}{L_0} + \left(\frac{\Delta L}{L}\right)_{\text{lit}}^{\text{Cu}}(T), \quad (0.7)$$

where $\Delta L_{\text{sample}}^{\text{meas}}$ is the measured response of the sample, $\Delta L_{\text{empty cell}}$ accounts for the background of empty cell, and $(\Delta L/L)_{\text{lit}}^{\text{Cu}}$ is the literature thermal expansion of copper. The empty-cell contribution is determined from measurements performed on a pure copper block with the same length as the YbRh_2Si_2 crystal. The in-plane relative length along the 100 and 110 crystallographic directions are shown in Fig. S4.

The linear thermal expansion coefficient $\alpha_i = \frac{d(\Delta L_i/L_{i,0})}{dT}$ along the direction i is obtained by calculating the numerical derivative of the normalized length change with temperature. Thermodynamically, the linear thermal expansion

$$\alpha_i = -(V_m)^{-1} \frac{\partial S}{\partial p_i} = (V_m Y)^{-1} \frac{\partial S}{\partial \epsilon_i}$$

probes the symmetry-conserving uniaxial pressure derivative of entropy S along the direction i , where V_m is the molar volume, which can also be expressed as symmetric strain derivative of the entropy, using Young's modulus Y .

Following [10], we derive a relation between the expansion coefficient and the symmetric elastoresistance, based upon the Fisher-Langer scaling relation for critical magnetic scattering in metallic magnets

$$\frac{\partial \rho}{\partial T} \propto C_{\text{mag}},$$

which relates the temperature derivative of the electrical resistance to the magnetic specific heat [34]. The temperature derivative of the linear thermal expansion

$$\frac{d\alpha_i}{dT} = (V_m Y)^{-1} \frac{\partial^2 S}{\partial \epsilon_i \partial T} = (V_m Y)^{-1} \frac{\partial}{\partial \epsilon_i} \frac{C}{T} \sim \frac{\partial}{\partial \epsilon_i} \frac{1}{T} \frac{\partial \rho}{\partial T} \sim \frac{1}{T} \frac{\partial(m_i R(T)/R_{300\text{K}})}{\partial T}$$

can thereby be expressed by the temperature derivative of the symmetric elastoresistance. It follows that

$$\alpha_i \sim \int \frac{1}{T} \frac{\partial(m_i R(T)/R_{300\text{K}})}{\partial T} dT + \text{const.} \quad (0.8)$$

the temperature dependence of thermal expansion follows that of the above integral.

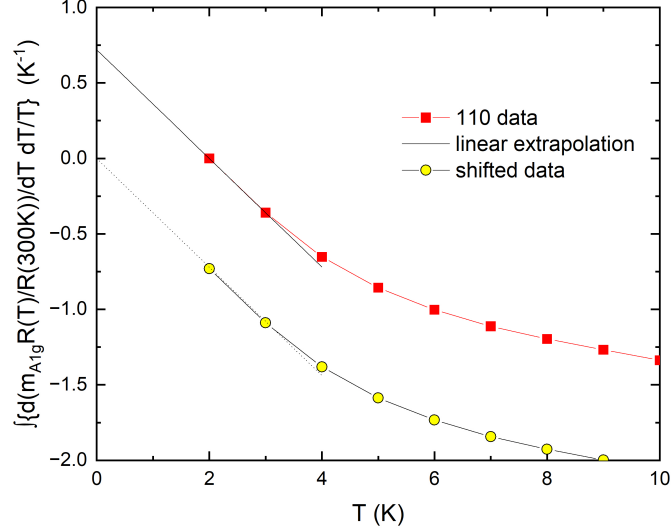


Figure S5. Temperature dependence of the intetragal from Eq.(S8) (red squares), starting at a temperature of 2 K. The black line indicates a linear fit through the data points at 2 and 3 K. It extrapolates to a value of 0.74 at $T = 0$. The yellow circles display shifted data (the red squares are subtracted by 0.74), yielding a linear extrapolation to zero at $T = 0$. Note, that for the [100] direction (not shown) a shift of 0.72 was used.

Since our data start at a temperature of 2 K, the integral starts at this temperature and has a value of zero at 2 K. However, a true thermal expansion has to extrapolate to zero at zero temperature. We therefore adjusted the integration constant to ensure that such extrapolation holds. As shown in Figure S5, this is realized by shifting the data from the integral by subtraction of an integration constant in Eq.(S8). Using a linear fit between the first two data points, the integration constant in Eq.(S8) was chosen to -0.74 (for the data along [110]) and -0.72 (for the data along [100]). The so derived “Fisher thermal expansion” has been divided by temperature and is plotted in the inset of Fig. 5 of the main text (see the further discussion in the main text). Without integration constant, this property would show a minimum below 10 K and approach zero at 2 K, but there is no reason why at this temperature the magnetic entropy would not show a strain dependence anymore. In fact, the measured thermal expansion coefficient displays a huge value of α/T at this temperature. Therefore, we believe that the integration constant shall not be neglected and the above determination of the constant by linear extrapolation to zero at $T = 0$ is the simplest way for the adjustment.